Tectonics

RESEARCH ARTICLE
10.1029/2021TC006828

Key Points:

- A simple thermal lithosphere-asthenosphere boundary (LAB) model for the South Atlantic passive margins has been developed
- The LAB model shows distinct variations along the margins that correlate with margin widths
- Conjugate margin pairs reflect an asymmetry in LAB depth patterns that are locally related to post-breakup lithospheric thinning

Supporting Information:

Supporting Information may be found in the online version of this article.

Correspondence to:

P. Haas,
peter.haas@ifg.uni-kiel.de

Citation:

Haas, P., Müller, R. D., Ebbing, J., Finger, N.-P., Kaban, M. K., & Heine, C. (2022). Modeling lithospheric thickness along the conjugate South Atlantic passive margins implies asymmetric rift initiation. *Tectonics*, *41*, e2021TC006828. https://doi.org/10.1029/2021TC006828

Received 23 MAR 2021
Accepted 25 AUG 2022

Modeling Lithospheric Thickness Along the Conjugate South Atlantic Passive Margins Implies Asymmetric Rift Initiation

Peter Haas[1], R. Dietmar Müller[2], Jörg Ebbing[1], Nils-Peter Finger[3,4], Mikhail K. Kaban[3], and Christian Heine[5]

[1]Institute of Geosciences, Kiel University, Kiel, Germany, [2]Earthbyte Group, School of Geosciences, The University of Sydney, Sydney, NSW, Australia, [3]GFZ German Research Centre for Geosciences, Potsdam, Germany, [4]Free University of Berlin, Berlin, Germany, [5]Specialist Geosciences, PTD/E/F, Shell Global Solutions International B.V, Rijswijk, The Netherlands

Abstract The lithospheric architecture of passive margins is crucial for understanding the tectonic processes that caused the breakup of Gondwana. We highlight the evolution of the South Atlantic passive margins by a simple thermal lithosphere-asthenosphere boundary (LAB) model based on onset and cessation of rifting, crustal thickness, and stretching factors. We simulate lithospheric thinning and select the LAB as the $T = 1{,}330$°C isotherm, which is calculated by 1D advection and diffusion. Stretching factors and margin geometry are adjusted to state-of-the-art data sets, giving a thermal LAB model that is especially designed for the continental margins of the South Atlantic. Our LAB model shows distinct variations along the passive margins that are not imaged by global LAB models, indicating different rifting mechanisms. For example, we model up to 200 km deep lithosphere in the South American Santos Basin and shallow lithosphere less than 60 km in the Namibe Basin offshore Africa. These two conjugate basins reflect a strong asymmetry in LAB depth that resembles variations in margin width. In a Gondwana reconstruction, we discuss these patterns together with seismic velocity perturbations for the Central and Austral Segments of the margins. The shallow lithosphere in the Namibe Basin correlates with signatures of the Angola Dome, attributed to epeirogenic uplift in the Neogene, suggesting an additional component of post-breakup lithospheric thinning.

Plain Language Summary Passive margins mark the transition zone from a continent to the ocean without being an active boundary of tectonic plates. They are typical for all continents on the globe. In the South Atlantic, the passive margins are located adjacent to the eastern coastline of South America and the western coastline of Africa. Studying the architecture of passive margins is essential for understanding plate tectonic history of the earth because they define how the continents once fitted together and how they broke apart. Passive margin segments on opposite sides of an ocean form so called conjugate margin pairs. Most geophysical studies of passive margins focus on the first few kilometers under the surface. However, their deeper extension to the base of the rigid shell of the earth, known as lithospheric thickness, is to a large extent unknown. Based on a simple temperature model, we find that the lithospheric thickness is highly variable and shows large variations along the South Atlantic passive margins. These differences are associated with the extension of conjugate margin pairs: where one margin is narrower than the conjugate, its lithospheric thickness is greater. This asymmetry indicates that the geodynamic processes, causing the breakup of the two continents, must have been asymmetric as well. Offshore Angola, the lithosphere is modeled shallow and matches with relatively young rock signatures. This suggests additional tectonic activity on the African side after the breakup between the two continents occurred.

1. Introduction

The architecture and evolution of passive margins have been extensively studied over the last decades (e.g., Geoffroy, 2005; Lister et al., 1986; Peron-Pinvidic & Manatschal, 2019; Reston, 2009). For a long time, this has been predominantly motivated by hydrocarbon exploration because numerous oil and gas occurrences are connected to passive margin formation. In recent years, passive margins have become focus for interdisciplinary and environmental studies (Peron-Pinvidic & Manatschal, 2019), like sequestering carbon dioxide (e.g., Ringrose & Meckel, 2019) or estimating the global carbon dioxide budget over deep time (e.g., Brune et al., 2017). In this study, we address the deep structure of passive margins and develop a new lithosphere-asthenosphere boundary

(LAB) model, which is specially designed for the South Atlantic passive margins and images the thermal structure of the lithosphere.

Passive margins are the end-member of rifting, where parts of the crust and lithosphere diverge from each other, accompanied by crustal and lithospheric stretching. The McKenzie model of rifting is a widely accepted model that explains uniform thinning of the continental crust and lithosphere by instantaneous stretching in pure shear mode, followed by thermal subsidence (McKenzie, 1978). Jarvis and McKenzie (1980) introduced a time-dependent analytical model that relates variations in heat flow and subsidence history to the rate of extension. In a traditional view, the formation of nonvolcanic passive margins were attributed to passive upwelling of buoyant sublithospheric mantle material, driven by far field extension forces, for which the McKenzie rifting model is chosen (Geoffroy, 2005; Sengör & Burke, 1978). Contrary to that, volcanic passive margins have been interpreted as the result of active upwelling of a mantle plume, associated with a thick crust due to magmatic underplating and the formation of Seaward Dipping Reflectors (SDRs; e.g., Geoffroy, 2005; Mutter et al., 1982). The occurrence of volcanic rifted margins does not necessarily require a pronounced thermal anomaly in the mantle related to a plume (e.g., Bown & White, 1995), but can be explained with transient small-scale mantle convection underneath the lithosphere (Nielsen, 2002; Simon et al., 2009) or plume-rift interaction (Morgan et al., 2020).

Numerous studies over the last years have shown that architecture of passive margins is more complex than previously thought (Peron-Pinvidic & Manatschal, 2019). The strict division between volcanic and nonvolcanic passive margins can no longer be maintained and passive margins should rather be characterized by their magmatic content as magma-rich versus magma-poor (Franke, 2013; Peron-Pinvidic & Manatschal, 2019). Tugend et al. (2018) propose that timing of decompression melting may be more important than estimates of the magmatic budget of passive margins to understand their evolution and variability. Another important observation is the asymmetry in the width of conjugate margin pairs (Brune et al., 2014; Svartman Dias et al., 2015). Early models explaining margin asymmetry are based on simple shear (Wernicke, 1981), which generates detachment faulting along low-angle normal faults, cutting through the entire lithosphere (Lister et al., 1986). In contrast, Brune et al. (2014) showed that margin asymmetry can instead be generated by rift migration, causing the development and lateral migration of a low viscosity pocket between upper and lower crust into which the faults are detaching. There is consensus that crustal and mantle processes interact during passive margin formation. However, the contribution of the mantle lithosphere in these processes is to a large amount unconstrained (Peron-Pinvidic & Manatschal, 2019).

In this study, we focus on the lithospheric structure of the South Atlantic passive margins, which are characterized by a wide range of different margin types. Triassic dyke swarms and rift basins may indicate earliest tectonic extensional forces (Borsa et al., 2017; Clemson et al., 2007; Peyve, 2010). However, it is unclear whether these structures are directly related to the subsequent extension and opening of the South Atlantic. In the Late Jurassic, rifting started and caused the disintegration of Western Gondwana, leading to the opening of the Falkland and Austral Segments of the South Atlantic (e.g., Heine et al., 2013; Moulin et al., 2010; Rabinowitz & LaBrecque, 1979). Rifting propagated northward, forming the Central Segment in the Aptian, which is positioned between the Rio Grande Fracture Zone in the south and the Chain Fracture Zone (CFZ) in the north (Moulin et al., 2010). In the Late Aptian/Early Albian, the equatorial part of the South Atlantic opened (Heine & Brune, 2014; Moulin et al., 2010), characterized by a higher degree of oblique rifting (Brune et al., 2018).

In recent years, several global and regional lithospheric thickness models have been published that cover the South Atlantic passive margins. Global models are, for example, derived from surface-wave dispersion maps (Pasyanos et al., 2014), conversion of seismic tomography to thermal LAB (Steinberger & Becker, 2018) or multi-probabilistic joint inversion (Afonso et al., 2019). The global LAB models have a wide depth range, partly depending on the data sets and regularizations used in establishing the models. Due to the narrow and elongated margin geometry, many of these global models are not capable of mapping the LAB in this region. Finger et al. (2021) presented a regional model for the South American continent based on combined density, thermal, and compositional modeling. However, their modeling approach focusses on the continental platform and the passive margins are not precisely represented.

We model the thermal evolution of lithosphere during rifting in the South Atlantic and define a LAB depth after rifting ceased, representing the present-day LAB depth. Our model is specially designed for the margin area of the South Atlantic. The thermal LAB depth is derived from three input parameters: stretching factors, duration of rifting, and crustal thickness. Stretching factors are calculated by dividing unthinned crust by thinned crust, using published crustal models. Together with duration of rifting and crustal thickness, we then calculate a thermal model of the

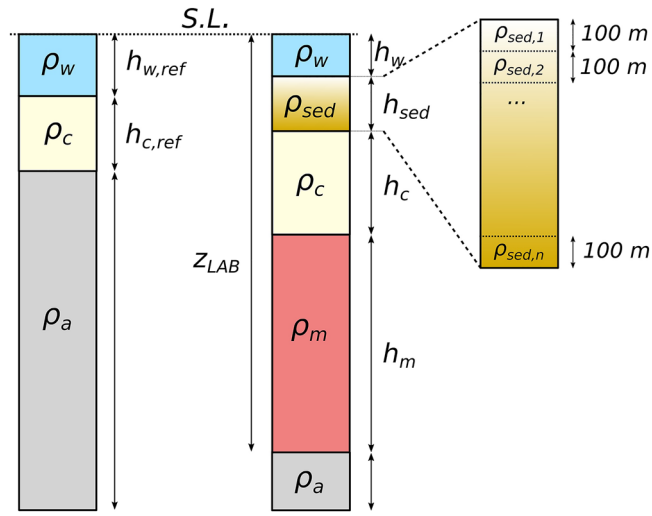

Figure 1. Isostatic balance of Mid-Ocean-Ridge (left) and passive margin (right). Mantle density ρ_m and thickness of mantle lithosphere h_m are the unknown parameters. Note that sediment density varies vertically. Full names of the parameters are given in Table 1.

extended lithosphere. The present-day LAB depth is defined by extrapolating the linear geotherm from the crust throughout the lithosphere after rifting and lithospheric cooling. Next, we discuss the evolution of the thermal LAB for the conjugate South Atlantic passive margins in a Gondwana reconstruction and evaluate differences between conjugate margin basins by correlating the predicted LAB depth with margin width and seismic tomography.

2. Methods

We calculate lithospheric thickness as a function of duration of rifting, crustal thickness, and stretching factors. For that, we use the python code *RiftSubsidence* based on a software that was originally designed to calculate theoretical subsidence curves for rifting scenarios in 1D (White et al., pers. com.). In *RiftSubsidence*, the subsidence is calculated based on the amount and timing of pure shear lithospheric extension, as well as on the thermal and density structure of the lithosphere, following the model of McKenzie (1978).

In this approach, the lithospheric thickness is derived from the thermal structure after the lithosphere has been stretched. The temperature of the model is calculated by 1D advection and diffusion using finite differences. The top of the model is defined at sea level, while the base of the model is defined as the LAB. At these boundaries, the temperature is fixed throughout the entire rifting period.

We adopt the duration of rifting as implemented in the deforming plate model of Müller et al. (2019). As simplification, early oceanic crust of the Austral and Central Segments of the South Atlantic are considered to be of the same age, ranging between 141 and 120 Ma (Müller et al., 2019). These two values represent onset and cessation of rifting for the Austral and Central Segments. At the Equatorial Segment, rifting initiated at 121 Ma and stopped at 107 Ma (Müller et al., 2019). Even though the exact timing of rifting may vary internally in each segment, the simplification is sufficient for application in thermal lithosphere modeling. In a synthetic example, we show that onset and cessation of rifting have the lowest impact on the modeled lithospheric thickness (Figure S1 in Supporting Information S1).

Prior to lithospheric stretching, LAB depth z_{LAB} and LAB temperature T_{LAB} must be defined. z_{LAB} is balanced isostatically against a reference Mid-Ocean-Ridge (MOR). Figure 1 shows the isostatic model of the reference MOR on the left and passive margin on the right. The vertical column of the passive margin is defined by five layers: water, sediments, crust, mantle lithosphere, and asthenosphere. Assuming that the thickness of the mantle lithosphere h_m is the only unknown parameter, an isostatic equation can be defined as follows:

$$h_m = \frac{\rho_w\,(h_{w,\mathrm{ref}} - h_w) - \sum_i^n \rho_{sed,i} \cdot 0.1\,\mathrm{km} + \rho_c\,(h_{c0} - h_c) + \rho_a\,(h_w + h_c + h_{\mathrm{sed}} - h_{c,\mathrm{ref}} - h_{w,\mathrm{ref}})}{(\rho_m - \rho_a)} \quad (1)$$

Table 1
Layers of Isostatic Model at Passive Margin With Respective Densities

Variable	Name	Value
ρ_w	Density of sea water	1.03 g/cm³
ρ_{sed}	Density of sediments	Variable[a]
ρ_c	Density of crust	2.81 g/cm³[b]
ρ_m	Density of lithospheric mantle	Unknown
ρ_a	Density of asthenosphere	3.3 g/cm³[c]
$h_{w,ref}$	Height of sea water at MOR	2.5 km[d]
h_w	Height of sea water	Variable[e]
h_{sed}	Height of sediments	Variable[f]
$h_{c,ref}$	Thickness of crust at MOR	7 km[g]
h_c	Thickness of crystalline crust	Variable[b,g]
h_m	Thickness of lithospheric mantle	Unknown

[a]Density of sediments calculated by isostatic equations of Sykes (1996). [b]Density and thickness of the crust for the continental part are taken from Finger et al. (2021). [c]Density of asthenosphere taken from Zoback and Mooney (2010). [d]Thicknesses of MOR reference column are taken from Afonso et al. (2019). [e]Water depth taken from ETOPO1 model. [f]Thickness of the sediments taken from the GlobSed-model of Straume et al. (2019). [g]Crustal thickness of the margin area is taken from the CRUST1.0 model (Laske et al., 2013).

The assumed values of density and thickness of each layer are listed in Table 1.

The densities of the sediments are calculated using depth-dependent equations provided by Sykes (1996), accounting for isostatic corrections of the sediment load. The sediment layers are vertically subdivided every 0.1 km. For each vertical column a density value is calculated, which contributes to the isostatic equation Equation 1.

The crustal thickness varies spatially for the passive margin. Accordingly, the LAB depth of the isostatic balance, from now on referred to as $z_{\mathrm{LAB,iso}}$, is individual for each point and is defined as $z_{\mathrm{LAB},iso} = h_w + h_{\mathrm{sed}} + h_c + h_m$. For crustal density, we calculate the average value over the margin area (see Table 1). The value of $\rho_c = 2.81$ g/cm³ is obtained by isostatically balancing thicknesses and densities of crystalline crust and sediments of the crustal model of Finger et al. (2021). Thus, it represents a mean value of the entire crust.

The isostatic balance in Equation 1 assumes a constant mantle density. As the South Atlantic passive margins are bounded by both continental and oceanic lithosphere, the mantle density is expected to be heterogeneous. Estimates from global and regional inversions indicate varying mantle densities along the South American passive margin (e.g., Afonso et al., 2019; Finger et al., 2021). Therefore, the mantle density is the second unknown parameter of the isostatic column.

Prior to rifting the thermal state of the lithosphere can be regarded as purely conductive with a linear geotherm. Assuming a constant linear geotherm for the entire lithosphere (blue lines in Figure 2), we calculate the mantle density and thickness of the mantle lithosphere in an iterative scheme:

1. Select a starting value of $h_{m,0}$. We select $h_{m,0} = 60$ km.
2. As the geotherm is linear throughout the lithosphere, the average mantle temperature $\overline{T}_m$ can be directly derived from T_{LAB} and the temperature at the Moho T_{Moho} is

$$\overline{T}_m = \frac{T_{\mathrm{LAB}} - T_{\mathrm{Moho}}}{2} \tag{2}$$

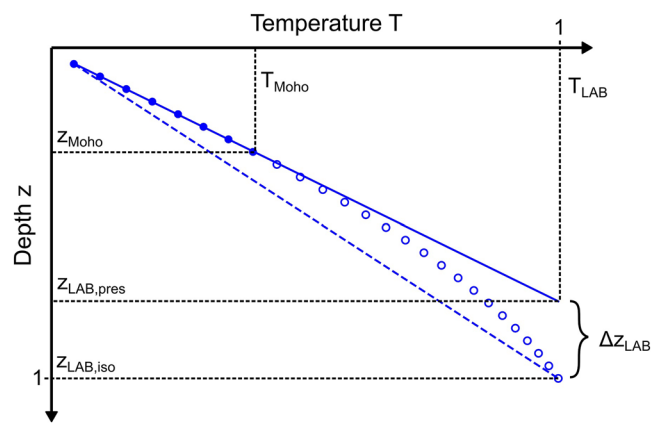

Figure 2. Geotherms and the lithosphere-asthenosphere boundaries. Dashed line: initial geotherm prior to onset of rifting, representing initial isostatic LAB depth $z_{\mathrm{LAB,iso}}$ and temperature at the LAB, T_{LAB}. Circles, uplifted geotherm after rifting and cooling; solid blue line, present-day extrapolated linear geotherm based on crustal thickness, z_{Moho}; and temperature at the Moho, thermal structure of crust (filled circles). The depth at which the extrapolated geotherm reaches T_{LAB} provides an approximate estimate of present-day lithospheric thickness $z_{\mathrm{LAB,pres}}$.

T_{Moho} can be substituted by the quotient of crustal and lithospheric thickness:

$$\overline{T}_m = \frac{T_{\text{LAB}}\left(1 + \frac{h_c}{h_c + h_{m,i}}\right)}{2} \tag{3}$$

With $h_{m,i}$ = thickness of mantle lithosphere at iteration step i.

3. Assume mantle density as a function of temperature, based on the volumetric coefficient of thermal expansion α (e.g., Turcotte & Schubert, 2018):

$$d\rho = -\rho\alpha dT \tag{4}$$

Solve the differential as follows:

$$\rho_a - \rho_{m,i} = -\rho_{m,i}\alpha\left(T_{\text{LAB}} - \overline{T}_m\right) \tag{5}$$

Solve Equation 5 for mantle density:

$$\rho_{m,i} = \frac{\rho_a}{1 - \alpha\left(T_{\text{LAB}} - \overline{T}_m\right)} \tag{6}$$

With $\rho_{m,i}$ = mantle density at the iteration step i.

4. Update h_m based on Equation 1 and mantle density of Equation 6.
5. Repeat Step 2–4.

The process is iterated until the density change reaches the threshold $\|\rho_{m,i+1} - \rho_{m,i}\| < 0.001$ g/cm³. For T_{LAB} and α, we choose standard values of T_{LAB} = 1,333°C and $\alpha = 3.28{*}10^{-5}$ 1/K (e.g., Jarvis & McKenzie, 1980; Parsons & Sclater, 1977).

$z_{\text{LAB,iso}}$ represents the depth of the LAB prior to rifting. If the lithosphere is not stretched, a linear geotherm can be assumed for the entire lithosphere. However, rifting causes lithospheric extension with subsequent nonlinear displacement of the geotherm. After extension ceases, the lithosphere cools and the geotherm relaxes back to the linear state at infinite time. Depending on initiation and end of rifting and the amount of stretching, the geotherm will deviate from its initial linear state (Figure 2).

In this approach, we simplify the geothermal gradients inside the lithosphere after rifting ceased. Assuming that conductive heat transport in the crust is the dominant heat source and that thermal expansion is constant both for the crust and lithosphere, we can extrapolate the geotherm of the crust throughout the mantle lithosphere. As a result, $z_{\text{LAB,iso}}$ is shifted upward (Figure 2). The difference between the initial $z_{\text{LAB,iso}}$ and present-day lithospheric thickness $z_{\text{LAB,pres,}}$, based on the extrapolated crustal geotherm, is defined as Δz_{LAB}. $z_{\text{LAB,pres}}$ defines the LAB depth after rifting ceased and the lithosphere has been cooling down.

The amount of nonlinearity of the distorted geotherm in Figure 2 depends on the elapsed time and on the amount of stretching. Based on the concepts described by McKenzie (1978), we define the stretching factor β as the thickness of unthinned crust divided by the thinned crust:

$$ß = \frac{h_i}{h_s} \tag{7}$$

h_i defines the initial crustal thickness, whereas h_s is the crustal thickness after stretching.

Müller et al. (2019) used this approach to derive stretching factors globally for all deforming regions. However, their values are calculated based on uniform stretching and do not consider crustal thickness gradients.

Synthetic tests show that stretching factors and crustal thickness have the largest impact on the modeled LAB depth (Figure S1 in Supporting Information S1). Therefore, we derive new stretching factors for the South Atlantic passive margins. The proximal extension of the passive margins is defined by the landward limit of stretched

continental crust, referred to as unstretched continental crust limit (UCCL; Williams et al., 2011). Here, we use the extension as it is captured in the deforming plate model of Müller et al. (2019). The distal extension of stretched continental crust is defined as landward limit of oceanic crust (LaLOC; Heine et al., 2013). We use the LaLOC geometry of the plate kinematic model of the South Atlantic (Heine et al., 2013), as it better integrates regional crustal-scale seismic data. Where SDRs sequences go beyond the margin area, hyperextended crust can be expected. Therefore, we adjust the geometry of the LaLOC by acknowledging the recently imaged SDR sequences for the Austral Segment of the passive margins (Chauvet et al., 2021; McDermott et al., 2018). This gives us the final geometry of the passive margin area, which is from now on referred to as continent-ocean-transition (COT) zone.

For the calculation of the stretching factors, we consider the thickness of crystalline crust by removing water and sediment layers (Figure S2 in Supporting Information S1). Two different crustal models are used: one for the inner continent, representing unthinned crust h_i, and one for the COT, representing thinned crust h_s. To obtain unthinned crust h_i, the inner margin of the COB is extended 500 km toward the continent. For South America, we select the continental crustal thickness model of Finger et al. (2021), which is based on a geostatistical kriging approach using available seismic determinations. For Africa, we use the CRUST1.0 model (Laske et al., 2013). Based on crustal thickness patterns and the distribution of tectonic domains, we define different segments and calculate mean values for each segment. This is sufficient for a first-order approximation of crystalline crustal thickness of unthinned crust, which is required for the estimation of stretching factors.

For thinned crust in the COT, we select the CRUST1.0 model in a resolution of 0.5° for both margins. To ensure a smooth transition to oceanic crust, we seed synthetic points in ~50 km distance along the LaLOC with a thickness of h_s = 8 km, representing average thickness of oceanic crust (Figure S3 in Supporting Information S1). Figures 3a and 3c show the crystalline crust for both margins and the inner extension area. The resulting stretching factors (Figures 3b and 3d) are discussed in the next section.

3. Results and Discussion

3.1. LAB Structure Along the South Atlantic Passive Margins

Figure 4 shows the modeled $z_{\mathrm{LAB,pres}}$ for the South Atlantic passive margins. The Rio Grande Fracture Zone (RGFZ) separates the Austral and Central Segments of the South Atlantic, while the CFZ separates the Central and Equatorial Segments (Moulin et al., 2010). As a general trend for both margins, $z_{\mathrm{LAB,pres}}$ is getting deeper toward the UCCL and shallower toward the LaLOC. However, the along-margin and across-margin patterns of $z_{\mathrm{LAB,pres}}$ vary for the different segments and basins of the South Atlantic passive margin.

Along the Austral Segment of the South American passive margin, the LAB depth reflects intermediate depths from 90 to 120 km (Figure 4a). In this area, only minor across-margin gradients in lithospheric thickness are modeled. In some parts of the Colorado and Punta del Este Basins, the modeled $z_{\mathrm{LAB,pres}}$ is almost flat, reflecting values at around 100 km depth. Toward the Santos Basin, the variation of $z_{\mathrm{LAB,pres}}$ is getting stronger. Along a wide COT area, the LAB deepens up to 180 km depth toward the UCCL. For the Central Segment, $z_{\mathrm{LAB,pres}}$ is uplifted up to 40 km toward the LaLOC, resulting in pronounced across-margin gradients. This is evident for the narrow Bahia Basin and the northward continuing Sergipe Alagoas Basin, where the range of $z_{\mathrm{LAB,pres}}$ varies from 40 to 200 km. In this area, the UCCL is extensively shifted toward the inland Borborema Province, which hosts isolated Early Cretaceous rift basins, causing lithospheric deformation during the opening of the South Atlantic (Heine et al., 2013). Compared to the Central and Austral Segments most parts of the Equatorial Segment are characterized by a deeper $z_{\mathrm{LAB,pres}}$ toward the UCCL. Only the narrow Potiguar and Barreirinhas Basins reflect a very shallow $z_{\mathrm{LAB,pres}}$ of 40–80 km. For the northward continuing Foz do Amazonas–Marajo Basin the COT is widely characterized by deep lithosphere between 120 and 160 km, but with a sudden uplift to 40 km toward the LaLOC.

On the African side, large parts of the Austral Segment of the COT show characteristics in lithospheric thickness patterns similar to the South American side. For the Southwest African Basin $z_{\mathrm{LAB,pres}}$ reaches values from 120 to 140 km (Figure 4b). However, an important difference to the South American conjugate is the distinct thinning of $z_{\mathrm{LAB,pres}}$ toward the LaLOC, similar to parts of the Equatorial Segment of South America. This lithospheric pattern is maintained along the Central Segment, independent of the margin widths. In some parts, the UCCL cuts through the adjacent Congo Craton, resulting in values of $z_{\mathrm{LAB,pres}}$ deeper than 150 km. Similar to the Borborema

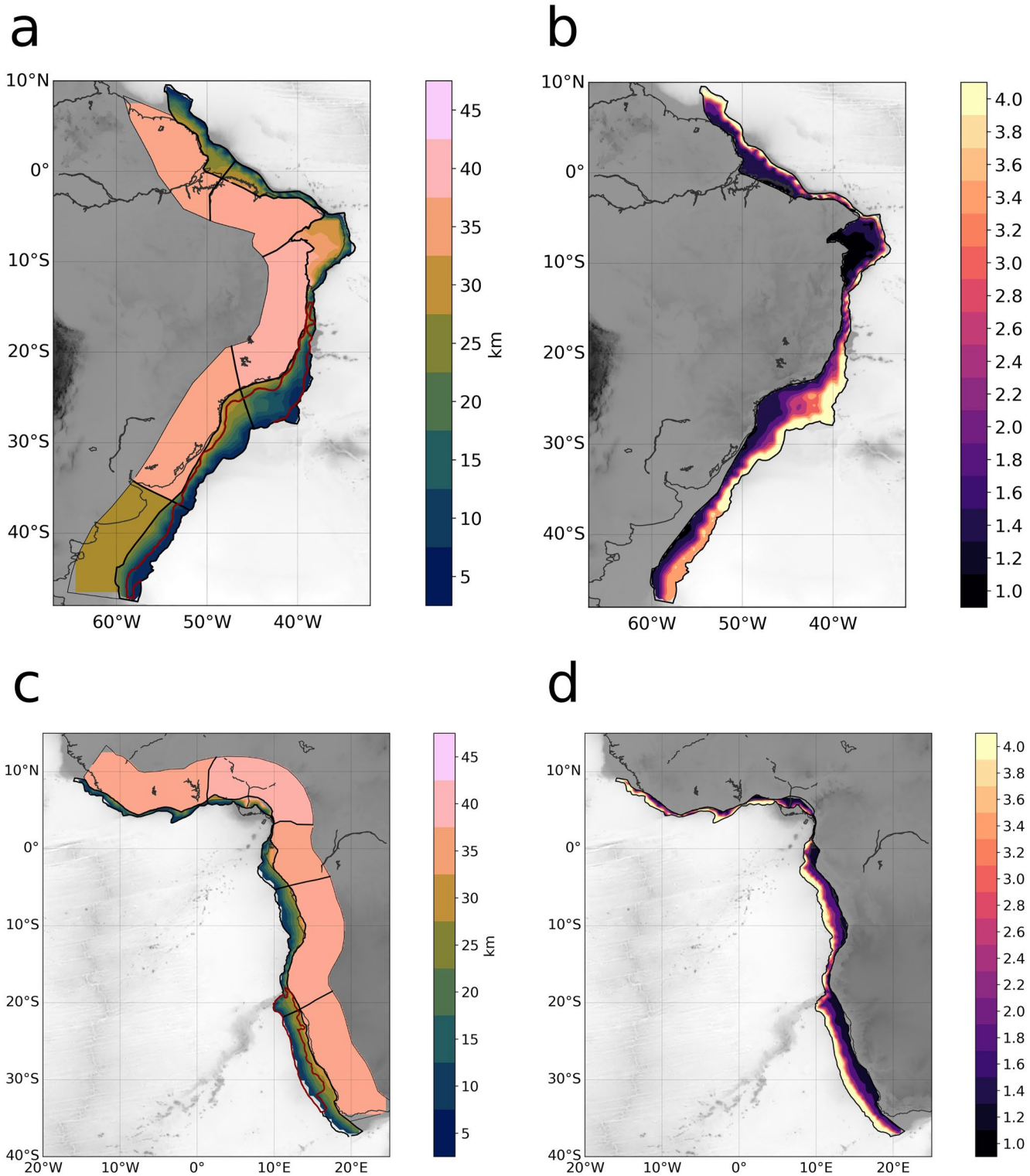

Figure 3. Thickness of crystalline crust and stretching factors for both continental margins. Thick black polygon defines continent-ocean-transition (COT), thin polygons the inner extension area. The gray-scale background plot shows topography. Dark-red polygons depict extension of Seaward Dipping Reflectors and Large Igneous Provinces (Chauvet et al., 2021; Coffin et al., 2006; McDermott et al., 2018). South American passive margin—(a)crystalline crustal thickness for COT and inner extension area and (b) estimated stretching factors. African passive margin—(c) crystalline crustal thickness for COT and inner extension area and (d) estimated stretching factors.

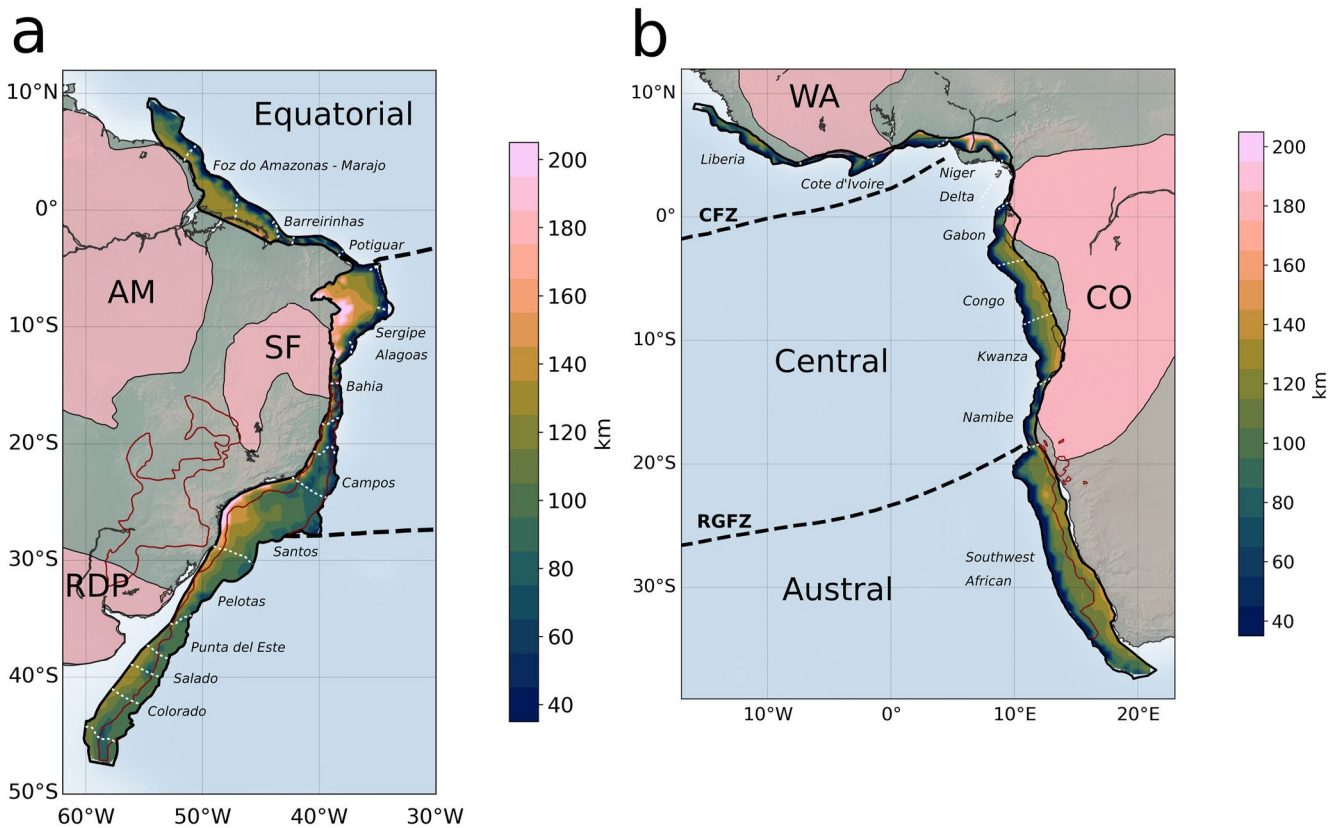

Figure 4. Present-day lithospheric thickness $z_{LAB,pres}$ for the South Atlantic passive margins. (a) South American passive margin and (b) African passive margin. Solid black lines indicate the extension of the continent-ocean-transition (COT) area. White dotted lines mark the boundaries of offshore sedimentary basins, taken from the Sedimentary Basins of the World database (Robertson CGG, 2017). Basin names are labeled in the figures. Thick dashed black lines indicate fracture zones, separating Equatorial, Central, and Austral Segments of the passive margins. CFZ = Chain Fracture Zone and RGFZ = Rio Grande Fracture Zone. Dark-red polygons mark the portion of the COT, which is characterized as Seaward Dipping Reflectors (SDRs, see Section 2). The onshore dark-red polygons highlight the Parana-Etendeka Large Igneous Province (LIP), taken from the Johansson et al. (2018) database. Filled coral polygons mark the location of cratons. South American Cratons: AM = Amazonia, SF = Sao Francisco, and RDP = Rio de la Plata. African cratons: WA = West Africa, CO = Congo.

Province, the COT in this area represents extended lithosphere along reactivated basement structures (Heine et al., 2013). At the northern boundary of the Central Segment, both UCCL and LaLOC are located onshore. In this area, the determination of the COT is inaccurate due to ongoing deposition of sediments in the Niger Delta, as well as overlapping signatures of the Central and West African Rift Systems, expressed as the Benue Trough. This causes large uncertainties in the modeled $z_{LAB,pres}$. These uncertainties are propagated throughout the Equatorial Segment, which is characterized by a very thin margin, challenging the identification of lithospheric structures both along and across the margin. For a comparison of conjugate margin segments in a Gondwana framework, we therefore focus on the Central and Austral Segments.

In Figure 5a, we show $z_{LAB,pres}$ rotated back to 115 Ma, together with depth profiles for selected conjugate margin pairs that are stitched together at the LaLOC of both margins (Figures 5b–5d). Thus, the value of maximum margin width corresponds to the location of the UCCL. For absolute comparison, we pick the LAB depth in the center of three selected margin profiles to show the lithospheric architecture across the margin:

1. Bahia/Congo margin.
2. Santos/Kwanza margin.
3. Salado/Southwest African Margin

We calculate the width of each passive margin profile by measuring the distance between the coordinates of UCCL and LaLOC, estimated by flowlines, which are implemented in the GPlates software (Müller et al., 2018). The conjugate Bahia/Congo Basins (Figure 5b) are characterized by a narrow margin of ca. 100 km width

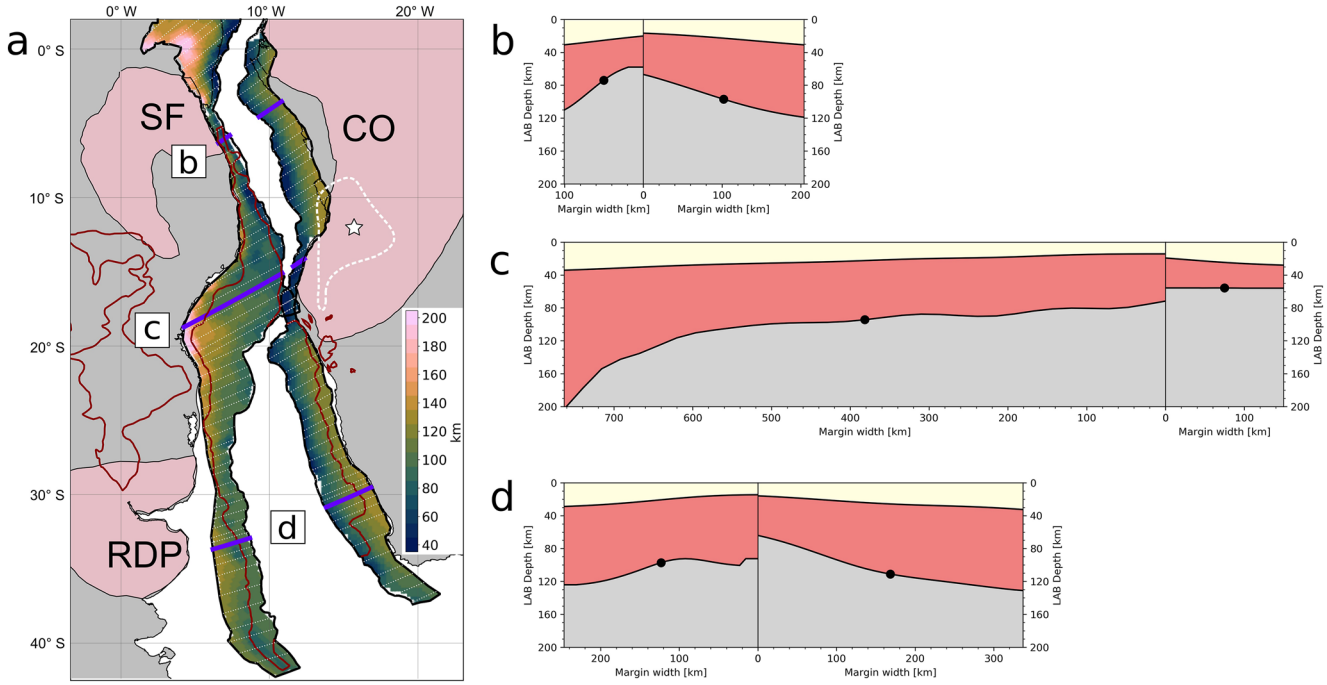

Figure 5. (a) Present-day lithospheric thickness $z_{LAB,pres}$ for the continent-ocean-transition (COT) area of the South American and African passive margins, rotated back to 115 Ma. Africa is fixed in present-day coordinates. Dark-red polygons mark the portion of the COT, which is characterized by Seaward Dipping Reflectors. The onshore dark-red polygons highlight the Parana-Etendeka Large Igneous Province, taken from the Johansson et al. (2018) database. Filled coral polygons mark the location of cratons. SF = Sao Francisco, RDP = Rio de la Plata, and CO = Congo. Thin white lines across the margins indicate extended flowlines to calculate the margin width. Thick violet lines mark selected margin profiles. White star represents the topographic high of the Angola dome and the white dashed line represents the +20 mGal bandpassed free air anomaly (Klöcking et al., 2020 and references therein). Right side: Selected margin profiles for conjugate basins. Light yellow layer represents crust, red layer mantle lithosphere, and gray layer asthenosphere. Thick black dot indicates the lithosphere-asthenosphere boundary depth at the center of each margin profile. (b) Bahia/Congo Basin, (c) Santos/Kwanza Basin, and (d) Colorado/Southwest African Basin.

on the South American side and an intermediate margin of 200 km width at the African counterpart. $z_{LAB,pres}$ varies between 80 km at the LaLOC and 120 km at the UCCL for the Congo Basin. For the Bahia Basin, the structure of $z_{LAB,pres}$ is similar, but 10 km shallower. Since the Bahia Basin is narrower than the Congo Basin, the across-margin gradient in $z_{LAB,pres}$ is more expressed. This gradient is already apparent in the initial stretching factors (Figure 3) and represents orthogonal rifting from the Base Aptian with a relatively constant thinning of $z_{LAB,pres}$ toward the LaLOC.

The Santos/Kwanza margin (Figure 5c) reflects a strong asymmetry with an ultra-wide margin on the South American side (more than 700 km) and a narrow margin on the African side (ca. 120 km). The asymmetry in this area has been attributed to steady state rift migration with larger extension velocity toward the Santos Basin (Brune et al., 2014), accompanied by an oblique orientation of rifting that results in very wide margin profiles across the Santos Basin. The asymmetry of the conjugate margin pairs is also reflected in the lithospheric structure across the margins. $z_{LAB,pres}$ varies between 70 and 200 km for the Santos Basin (Figure 5c). Given the enormous width of the Santos Basin, the across-margin gradient is rather smooth, especially for the first 550 km proceeding from the LaLOC, where $z_{LAB,pres}$ increases from 80 to 100 km. Just in the last 150 km toward the UCCL, $z_{LAB,pres}$ drops from 110 to 200 km depth. This deep lithosphere is already present in the isostatic LAB depth $z_{LAB,iso}$ (Figure 7a), due to thick crust (Figure 3a) and shallow water depth (Figure S2 in Supporting Information S1), which is only partially compensated by the thermal modeling. For the conjugate Kwanza Basin, $z_{LAB,pres}$ is in stark contrast to the South American counterpart. In this area, $z_{LAB,pres}$ is constant at around 55 km depth across the entire margin. However, since the Congo Craton directly borders to the Kwanza Basin, deeper cratonic lithosphere can be expected. One reason for the shallow lithosphere in the Kwanza Basin is higher stretching factors across the entire COT area (Figure 3d). Another reason might be Neogene epeirogenic uplift of the onshore Angola Dome (white star in Figure 5), which has been attributed to thermomechanical thinning of the lithospheric mantle (Klöcking et al., 2020). The distribution of the +20 mGal free air anomaly contour (white

dashed line in Figure 5) indicates that the dynamic support of the lithospheric mantle is located more southward of the Angola Dome. Together with our modeled $z_{LAB,pres}$, which represents the thermal state of the lithosphere, these observations provide evidence for post-breakup lithospheric thinning in this area.

As part of the Austral Segment, the conjugate Salado/Southwest African Basins represent an earlier rifting stage in the Early Cretaceous. Therefore, the margins already have diverged from each other at 115 Ma (Figure 5a). Rifting occurred presumably in orthogonal direction, and both margins are characterized by intermediate margin widths of moderate asymmetry, where the Salado Basin is 100 km narrower than the Southwest African Basin. A moderate asymmetry is also visible in the LAB structure with values from 90 to 120 km for the Salado Basin and 60–130 km for the Southwest African Basin. $z_{LAB,pres}$ in the center of the margin profiles is, however, similar for both margins (100–110 km), representing typical values for cooled oceanic lithosphere (e.g., Richards et al., 2020). The observed asymmetry is in agreement with a study of Chauvet et al. (2021), who relate the asymmetry of conjugate SDR sequences in the Austral Segment to variations in the thermal structure.

In comparison to the other input variables, the lateral variations of lithospheric thickness are caused by varying stretching factors. In our synthetic example, we show that the amount of stretching causes large variations in the modeled lithospheric thickness (Figure S1 in Supporting Information S1). As an approximation on global scale, Müller et al. (2019) showed stretching factors as part of their deforming plate model that represent "wide rifts that lack margin-orthogonal strain rate and crustal thickness gradients." Our approach is based on laterally varying crustal thickness. This is captured as along- and across-margin variations in the stretching factors (Figures 3b and 3d), making it an important enhancement of the stretching factors that are delivered with the Müller et al. (2019) deformation plate model. In most areas, stretching increases toward the LaLOC. Highest stretching factors are obtained close to or at the LaLOC. The maximum value of stretching is $\beta = 4.6$, implying that continental crust is almost five times thicker than the crust close the LaLOC. This is evident for large parts of the LaLOC of both margin sides (Figures 3b and 3d).

Thermal lithospheric thickness models are closely related to seismic tomography models. Assuming that variations in seismic velocities are only related to temperature variations, seismic tomography models can be converted to thermal LAB models (e.g., Cammarano et al., 2003; Steinberger & Becker, 2018). Therefore, we qualitatively compare seismic velocities from S-wave tomography (Celli et al., 2020), LAB depths, and conjugate margin widths for the Central and Austral Segments (Figure 6b–6d). In general, margin width is proportional to LAB depth, that is, a thin margin corresponds to shallow LAB depth. Only the LAB depth in the center of the South American Santos Basin deviates from this trend. The patterns in seismic tomography, however, are different.

For the African part of the Austral Segment, LAB depths from 90 to 110 km correspond to slight perturbations in S-wave velocity dV_s around −0.5% to 0%. Along the South American margin, the imaged $z_{LAB,pres}$ is similar to the African part, but the across margin distribution and velocity pattern changes (light gray areas in Figures 6c and 6d). In addition, a high velocity anomaly between 2% and 3.5% is observed, which is unusual for passive margin lithosphere. Celli et al. (2020) interpret the high velocities in this area by a deep lithospheric root, caused by isostatic negative buoyancy. The deeper across margin distribution of $z_{LAB,pres}$ indicates that there might be a contribution of lithospheric buoyancy. However, this area also coincides with compositional changes in the lithospheric mantle, which are not imaged by seismic tomography (e.g., Afonso et al., 2019). Our results indicate a combination of both thermal and compositional anomalies along the Austral segment of the South American passive margin.

Toward the Rio Grande Fracture Zone and the transition to the Central Segment, both $z_{LAB,pres}$ and dV_s deviate stronger. On the South American side, high velocity anomalies are maintained, coincident with a wide range of lithospheric thickness in the Santos Basin. Further north in the Campos and Bahia Basins dV_s drops to −1.5%, accompanied by shallower LAB depths (80–100 km). These structures might represent anomalously hot oceanic lithosphere due to activity of the Trindade Hotspot (Celli et al., 2020). At latitudes 5° S and further north, LAB depths between 60 and 160 km coincide with distinct velocity anomalies higher than 2%. Because the UCCL is shifted landward, these anomalies represent to a large extent continental lithosphere of the Borborema Province.

Strikingly, between latitudes 20° S and 15° S of the African passive margin, $z_{LAB,pres}$ and dV_s are anti-correlated. Very shallow lithosphere less than 60 km in the Namibe Basin is associated with a high velocity anomaly of 2%. At the transition to the northern Kwanza Basin, $z_{LAB,pres}$ increases, while dV_s drops to 0.5%. Only for latitudes north of 10° S, throughout the Congo and Gabon Basins, high velocity perturbations correlate with deeper lithosphere. Similar to our interpretation of the shallow lithosphere, the drop in S-wave velocity is related to a thermal

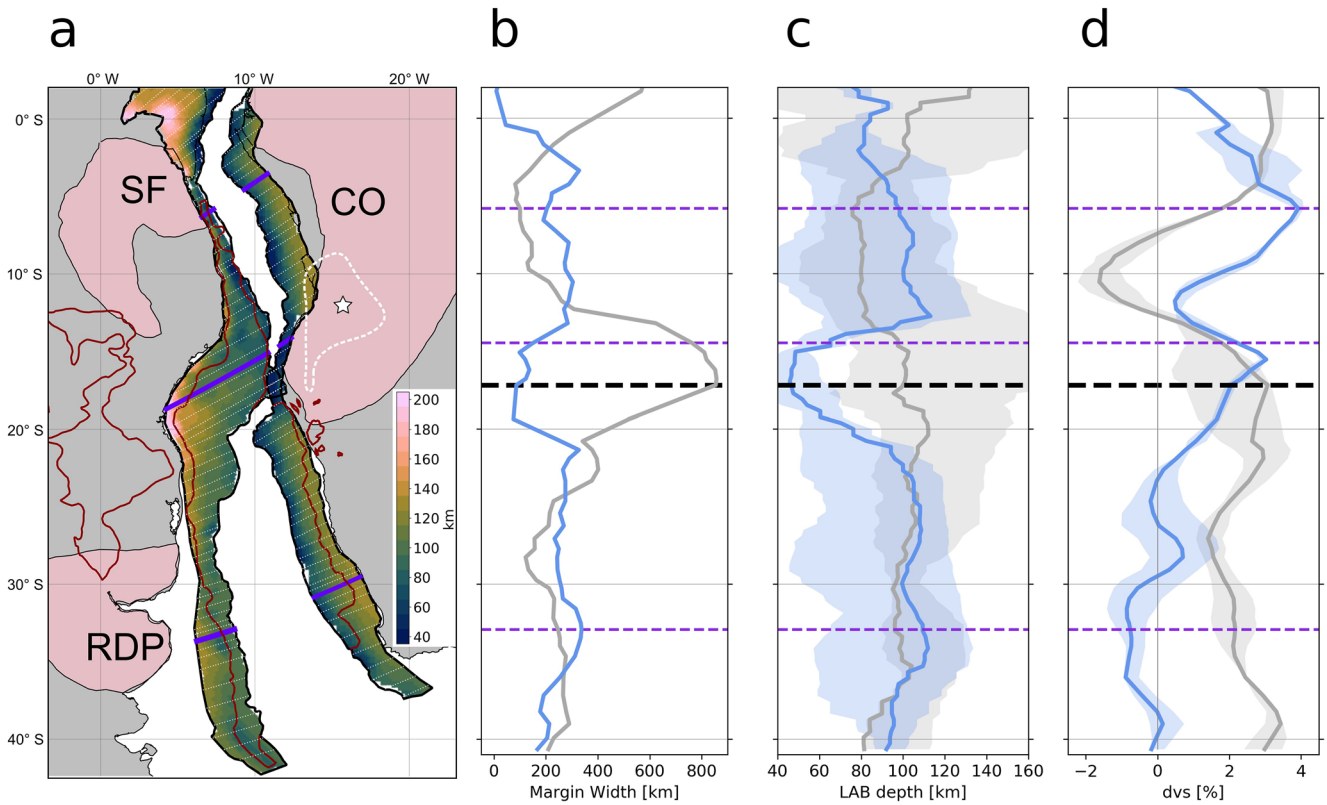

Figure 6. (a) present-day lithospheric thickness $z_{LAB,pres}$ for the continent-ocean-transition area of the South American and African passive margins, rotated back to 115 Ma. For details, see Figure 5. (b) Margin width versus Latitude for both conjugate margins. The latitude position of the conjugate margin pairs is picked at the LaLOC on the South American side. Gray, South America and Blue, Africa. Thick black dashed line indicates the position of the Rio Grande Fracture Zone, separating the Austral and Central Segments. Violet dashed lines mark the profiles shown in Figure 5. (c) lithosphere-asthenosphere boundary (LAB) depth versus Latitude. Solid lines indicate the LAB depth at the center of each margin profile. Transparent colors define the distribution of lithospheric thickness across the respective margin profile. (d) Seismic velocity anomaly versus Latitude. Solid lines indicate seismic velocity anomaly at the center of each margin profile. Transparent colors indicate the distribution of seismic velocity anomalies across the two margin sides.

anomaly in the lithospheric mantle, expressed as the Angola Dome (Klöcking et al., 2020). The anti-correlation between $z_{LAB,pres}$ and dV_s in this area less indicates a dichotomy of the two models, but rather a relative of a few hundred kilometers in north-south direction. In the South Atlantic Basins, the tomographic model has the lowest lateral resolution in the lithosphere (Celli et al., 2020). Therefore, horizontal smearing of seismic velocities can be expected. However, further research is required to explain the differences between our lithospheric model and seismic tomography in more detail.

3.2. Isostatic Balance and Ground Truthing of Crustal Thickness

To quantify the effect of linear extrapolation of the geotherm, $z_{LAB,iso}$ and the difference of $z_{LAB,pres}$ and $z_{LAB,iso}$, Δz_{LAB}, are calculated for the South American passive margin. We also investigate the estimated mantle density and number of iterations. Here, we show the results for the South American passive margin. Results for the African passive margin show similar features (Figure S4 in Supporting Information S1).

Many features of $z_{LAB,pres}$ are already present in $z_{LAB,iso}$ (Figure 7a). Across margin gradients of lithospheric thickness are established with shallower lithosphere toward the LaLOC. A prominent feature is the deep lithosphere along the Santos Basin and the continental Borborema Province. However, Δz_{LAB} reflects important differences, changing the structure of lithospheric thickness significantly. Highest values of Δz_{LAB} are 30 km and are found in the Santos Basin, the proximal part of the Bahia Basin and the distal parts of the Punta del Este, Salado, and Colorado Basins (Figure 7b). In the Central and Equatorial Segments, Δz_{LAB} decreases toward the LaLOC. Highest differences can be expected in regions with a low ratio between crustal thickness and isostatic thickness of the mantle lithosphere, because the difference between the linear geotherm approximation and the initial geotherm is

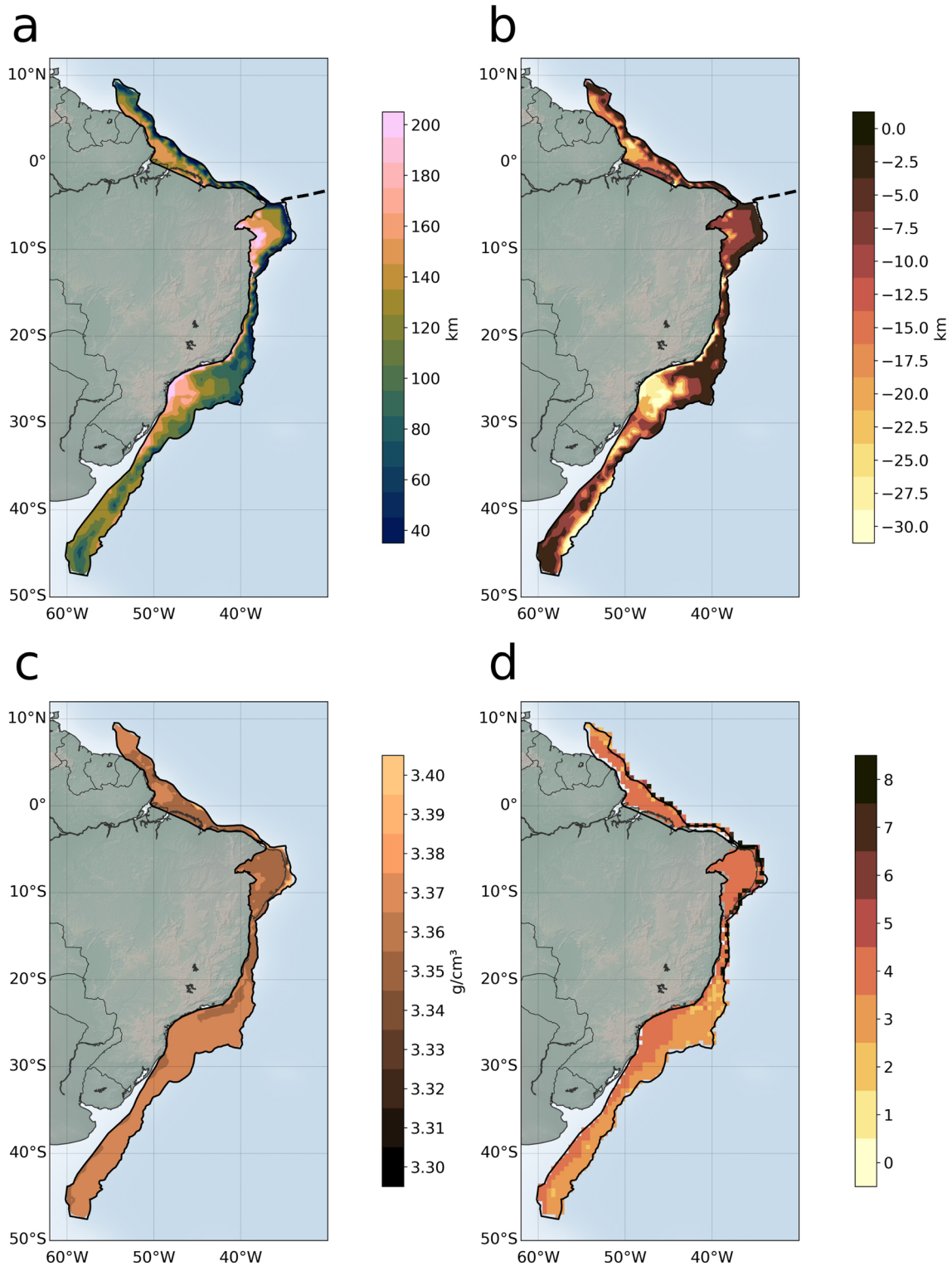

Figure 7. (a) initial isostatic lithosphere-asthenosphere boundary (LAB) depth prior to onset of rifting, $z_{\mathrm{LAB,iso}}$. (b) Difference of present-day LAB depth $z_{\mathrm{LAB,pres}}$ and $z_{\mathrm{LAB,iso}}$, Δz_{LAB}. (c) mantle density ρ_m, (d) number of iterations needed to satisfy density threshold.

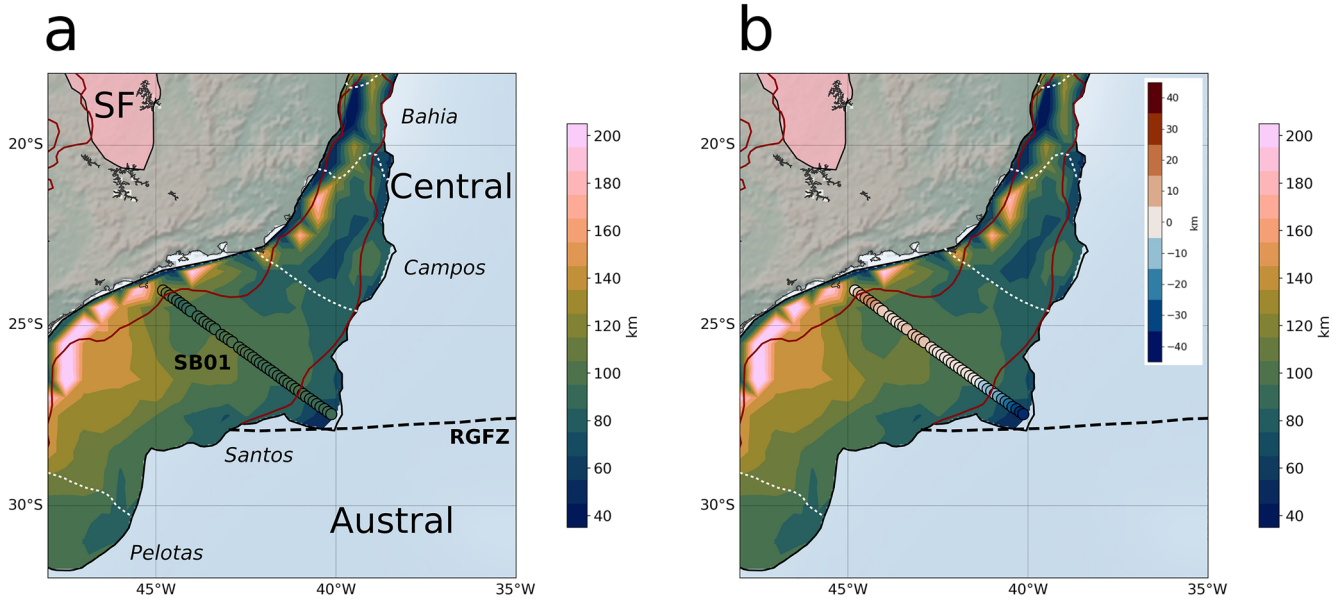

Figure 8. Modeled present-day lithosphere-asthenosphere boundary (LAB) depth $z_{LAB,pres}$ focused on the Santos Basin and its surroundings. White dots mark the boundaries of adjacent offshore basins. The dark-red polygon indicates the presence of Seaward Dipping Reflector sequences. (a) scattered points indicate $z_{LAB,pres}$ using crystalline crustal thickness values from an offshore wide-angle seismic profile SB01 (Evain et al., 2015). (b) same illustration as in **a**, but showing the differences of LAB depths between the gridded model, based on CRUST1.0 crustal thickness and interpolated onto the SB01 profile, and the scattered model, based on SB01 crustal thickness. Inset color bar shows the differences between the two models. SF= Sao Francisco Craton and RGFZ = Rio Grande Fracture Zone.

strongly expressed (see Figure 2). The Santos Basin is characterized by deep $z_{LAB,iso}$ up to 200 km and intermediate crustal thickness around 30 km and the distal part of the southern basins is characterized by very shallow crust less than 10 km (Figure 3a). Therefore, Δz_{LAB} is high in these regions. In the other regions, the difference of crustal thickness and isostatic thickness of the mantle lithosphere is too small to generate a significant variation in Δz_{LAB}. This is evident, for example, in large parts of the Pelotas and Bahia Basins.

The second unknown parameter of the isostatic balance is the mantle density ρ_m. Figure 7c displays the mantle density of the isostatic column prior to rifting. Notably, ρ_m is modeled 3.35–3.36 g/cm³ for most areas, which gives a difference of 0.05 g/cm³ compared to the density of the asthenosphere ρ_a (3.3 g/cm³). This reflects the temperature-dependent decrease of density with depth from lithosphere to asthenosphere. Most of the points reach the density threshold after $i \leq 4$ iterations (Figure 7d). Only where lithospheric thickness is very low, like in the distal part of the Equatorial Segment, the algorithm needs more iterations to converge. The results show an inherent stability between mantle density and thickness of the mantle lithosphere, which are the variable parameters of the isostatic balance.

Even though many studies of the crustal structure of the South Atlantic passive margins have been carried out, a coherent and consistent crustal model for the individual passive margins is not publicly available. Since our approach is designed on a continental scale, we select crustal thickness values from the global CRUST1.0 model (Laske et al., 2013). However, to acknowledge the continuous growth of available seismic refraction data that has been acquired in the last decades, we compare the modeled LAB depth $z_{LAB,pres,}$ based on CRUST1.0 crustal thickness data, to a modeled LAB depth, which is based on crustal thickness values for a given seismic refraction profile in the Santos Basin. We select the profile SB01, which is a wide-angle seismic profile that was acquired during the Santos Basin (SanBa) experiment in 2011 (Evain et al., 2015). By comparing both LAB models to the seismic profile, we can ground truth our modeled LAB depth.

For the isostatic calculation, we keep the other input parameters and data sets as listed in Table 1 and interpolate sediment thickness and water depth on the seismic profile. Stretching factors are recalculated by updating thinned crust with the crustal thickness values of Evain et al. (2015). The values for unthinned crust, as well as onset and cessation of rifting remain the same. The modeled LAB depth $z_{LAB,pres}$ at the SB01 profile reflects a very smooth structure with values between 90 and 110 km (Figure 8a), which is in accordance with the plate cooling model (Richards et al., 2020). Even toward the LaLOC this structure is maintained. Interpolating the previ-

ously estimated $z_{LAB,pres}$ onto the seismic profile gives the differences to the obtained values on the SB01 profile (Figure 8b). Toward the distal part of the Santos Basin, the gridded $z_{LAB,pres}$ is up to 40 km shallower than $z_{LAB,pres}$ on the seismic profile. In this area, synthetic crustal thickness of h_c = 8 km at the LaLOC may cause a bias toward shallower LAB depth. Nevertheless, the LAB structure of both modeling approaches is fairly similar. Differences are in a range between ±10 km throughout the vast part of the profile, illustrating that crustal thickness of the CRUST1.0 model is well-suited to model the LAB structure along the Santos Basin.

The Santos Basin is characterized by large SDR sequences, which vary in type and thickness across the margin, indicating a variable budget of magmatic material that was erupted during continental breakup (McDermott et al., 2018). The heterogeneity in SDR sequences is not reflected in the modeled LAB depths, neither in the gridded $z_{LAB,pres}$, nor in $z_{LAB,pres}$ along the SB01 profile. Therefore, a characterization of different SDR types and the subsequent determination of the magmatic budget remains a task that is beyond the resolution of the presented LAB depth models.

3.3. Comparison With Global LAB Models

While our lithospheric model is designed for passive margins only, other lithospheric models capture passive margins as part of a larger, in many cases global, model. In this section, the lithospheric thickness of our approach is compared to two global lithospheric models (Figure 9). The first model, LithoRef18, is derived by joint inversion of multiple data sets (Afonso et al., 2019). The second model from Steinberger and Becker (2018) is derived by conversion of seismic tomography to a thermal LAB. We used the mean LAB depth of several seismic tomography models as published in Steinberger and Becker (2018).

For LithoRef18, a two-part structure of deeper lithosphere in the Equatorial Segment and shallower lithosphere in the Central and Austral Segments can be observed (Figure 9a). Compared to our model, the across margin gradients of LAB depth are less pronounced. In general, the LAB of LithoRef18 is deeper than our model. Thicknesses up to 180 km at the Equatorial Segment are reached, which is 80 km deeper than our model (Figure 9b). Also, the Central Segment of LithoRef18 is 40–80 km deeper. As an exception, a shallow anomaly in the southern Santos Basin images lithospheric thickness of around 50 km. Controversially, this structure coincides with the deep anomaly of our lithospheric model. In the LithoRef18 model, this area is characterized by anomalously low densities in the lithospheric mantle (~3.27 g/cm³), forcing the LAB to be lifted up. In the Austral Segment, the difference in LAB depth between our model and LithoRef18 are in a range of ±40 km, indicating that both models image the same lithospheric structures. For the African margin, the differences are of the same magnitude as for the South American margin (Figure S5 in Supporting Information S1). With depths between 110 and 180 km the thermal LAB of Steinberger and Becker (2018) shows a smoother distribution of lithospheric thickness than the other two models (Figure 9c), representing the laterally coarse resolution and attenuation of global seismic tomography models. Values smaller than 100 km are not observed. In general, the distribution of lithospheric thickness is similar to LithoRef18. The most notable difference is the missing shallow lithosphere in the southern Santos Basin. In this area, the thermal LAB of Steinberger and Becker (2018) is very close to our model (Figure 9d).

Like in our model, the final LithoRef18 LAB strongly depends on the initial LAB assumptions. Afonso et al. (2019) used a hybrid model, based on six seismic tomographic models, including all models that Steinberger and Becker (2018) used plus the Litho1.0 model (Pasyanos et al., 2014). This explains similar lithospheric thicknesses for the vast extent of the passive margin. Afonso et al. (2019) used a weighted average, giving largest weights to Litho1.0 and SL2013sv (Schaeffer & Lebedev, 2013). The shallow lithosphere in the southern Santos Basin is a consequence of the preferred selection of Litho1.0, where shallow lithosphere is very pronounced.

Our model does not imply any preference which seismic tomography model should be used to convert seismic velocity to lithospheric thickness. As our model is purely thermal, pressure and compositional effects are not accounted for in the modeling process, whereas the presented global LAB models (partly) account for that. Our regional analysis rather shows a more variable structure of lithospheric thickness that global seismic tomographies cannot resolve due to their relatively coarse resolution. This makes our model relevant for studying the entire crustal and lithospheric architecture of passive margins, where tectonic signatures that are linked to lithospheric deformation vary on small scale.

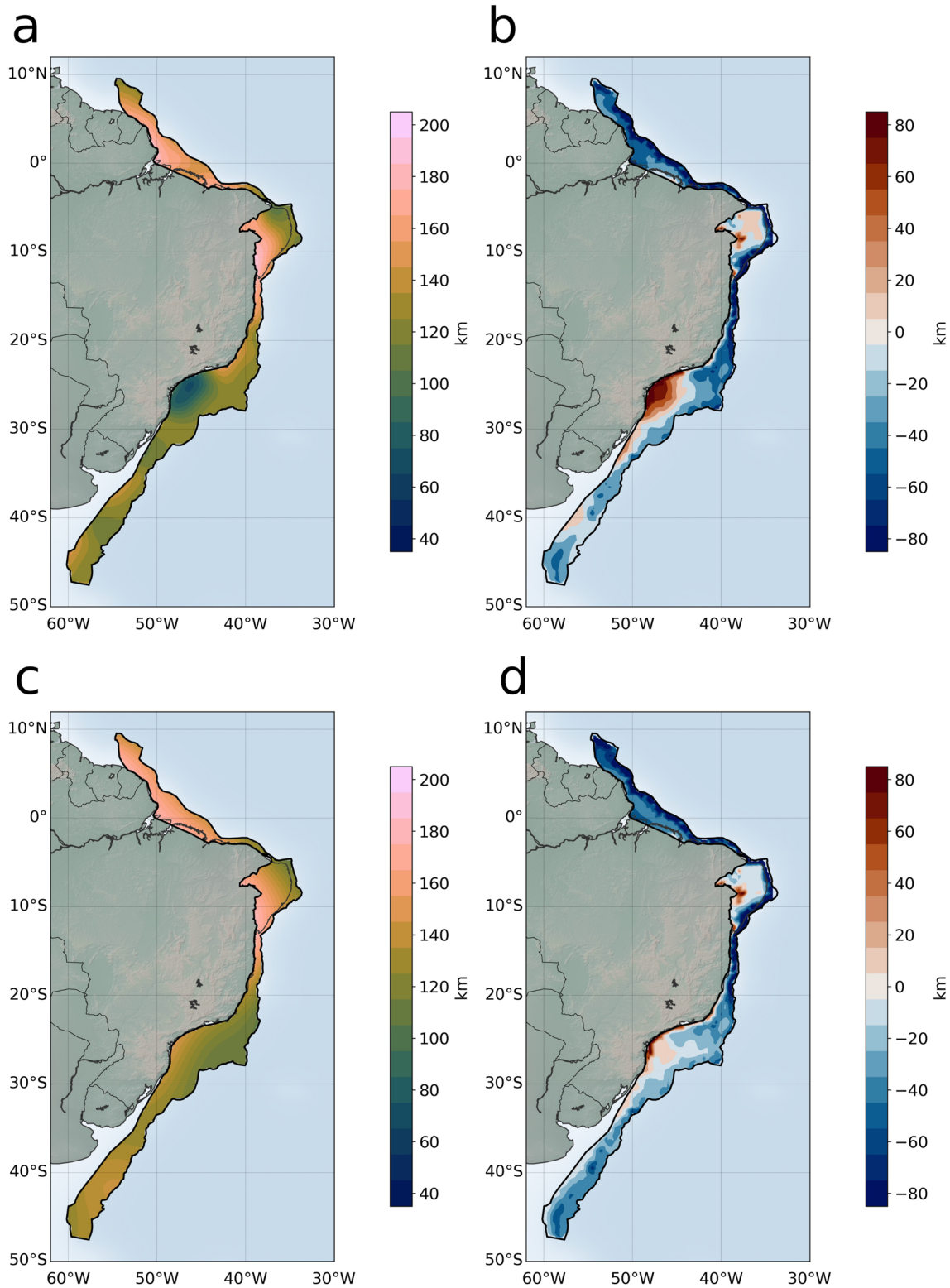

Figure 9. Lithosphere-asthenosphere boundary (LAB) thickness for the continent-ocean-transition area based on global models (on the left) and their differences to our model (on the right). (a and b) LithoRef18 (Afonso et al., 2019); (c and d) Mean LAB model of Steinberger and Becker (2018).

4. Conclusions

We have derived a new present-day thermal lithospheric thickness model for the South Atlantic passive margins. Our model is calculated as a function of onset and cessation of rifting, crustal thickness, and stretching factors. The stretching factors are obtained by dividing unthinned crust by thinned crust, using published crustal models for the South American and African continent. The new stretching factors account for across rift crustal gradients at the passive margin and are a refinement compared to the Müller et al. (2019) model.

From our model, the LAB structure along the South Atlantic is more precisely determined than from global models. We model distinct variations in LAB depth in the range of 40–200 km along and across the passive margins, indicating different rifting mechanisms that lead to the opening of the South Atlantic. As a general trend, the LAB deepens toward the proximal part and shallows toward the distal part of the margin area. The amplitude, however, varies for individual basins. In the Austral Segment of the South American basins, the LAB is rather constant between 90 and 110 km, whereas for the conjugate Southwest African Basin, the across-margin gradient is expressed by an abrupt shallowing toward the LaLOC.

Comparing the LAB depths along the margins with the width of margin profiles show a structural correlation: thin lithosphere coincides with narrow margins. Analyzing the LAB depth in a Gondwana reconstruction reveals an asymmetry for conjugate margin profiles. Significant differences in margin width correlate with significant differences in LAB depth for conjugate margin pairs. This is especially evident for the conjugate Santos/Namibe Basins, implying a substantial component of asymmetric rifting. As an additional factor, thin lithosphere in the Namibe Basin matches with signatures of the Angola Dome, indicating post-breakup lithospheric thinning. To which extent the Angola Dome contributes to lithosphere thinning remains unclear. The same holds for quantification of magmatic underplating, which is beyond the resolution of our LAB model.

Future efforts should address these open questions, once a comprehensive data set outlining underplated crustal thickness on both conjugate margins is available. This could be easily included in the governing isostatic equation. The modeling of the thermal structure can be extended to 2D rifting scenarios instead of the 1D approach that we are using. Given the potential of improvements, we are confident that our approach opens a new pathway for more extensive analysis of the lithospheric structure of passive margins. Our procedure can be easily adapted to other passive margins on the globe. Ultimately, this would fill the gaps of reconstructed lithospheric models for the Gondwana Supercontinent.

Data Availability Statement

Models of crustal thickness and density for South America are published via the GFZ Data Services: https://doi.org/10.5880/GFZ.1.3.2020.006 (Finger et al., 2021). The rifting times of the South Atlantic opening are part of the deforming plate model of Müller et al., 2019, which is available at: https://www.earthbyte.org/webdav/ftp/Data_Collections/Muller_etal_2019_Tectonics/. The code RiftSubsidence.py is available at Zenodo: https://doi.org/10.5281/zenodo.7074000 (EarthByte Group, 2022). The modelled lithospheric thickness, the input parameters, as well as a GPlates project to reconstruct the data in a Gondwana framework are available at: https://earthbyte.org/webdav/ftp/Data_Collections/Haas_etal_2022_Tectonics/. Most of the plots have been created using Matplotlib with color-blind friendly color maps (Crameri, 2018; Hunter, 2007).

Acknowledgments
This work has been funded by the Deutsche Forschungsgemeinschaft (DFG) within the project "Linking the deep structures of the cratons of Africa and South America by integrated geophysical modelling" (Project number 336717379). We thank Nicky White from University of Cambridge for sharing his FORTRAN code, which has been converted to Python by Michael Chin from University of Sydney. Gregory Houseman from Leeds University is thanked for his contributions to the code and for general discussions about thermal modeling. Furthermore, we thank Paul Bellingham from ION Geophysical for fruitful discussions on modeling lithospheric extension along passive margins. We are thankful for the valuable comments of Dale Bird and another reviewer. Open Access funding enabled and organized by Projekt DEAL.

References

Afonso, J. C., Salajegheh, F., Szwillus, W., Ebbing, J., & Gaina, C. (2019). A global reference model of the lithosphere and upper mantle from joint inversion and analysis of multiple data sets. *Geophysical Journal International*, *217*(3), 1602–1628. https://doi.org/10.1093/gji/ggz094

Borsa, G. N. O., Mizusaki, A. M. P., & Menegat, R. (2017). The Triassic belt preserved in Arroio Moirão Graben, southernmost Brazil: Depositional system, sequence stratigraphy and tectonics. *Journal of South American Earth Sciences*, *77*(2), 123–140. https://doi.org/10.1016/j.jsames.2017.05.002

Bown, J. W., & White, R. S. (1995). Effect of finite extension rate on melt generation at rifted continental margins. *Journal of Geophysical Research*, *100*(B9), 18011–18029. https://doi.org/10.1029/94JB01478

Brune, S., Heine, C., Pérez-Gussinyé, M., & Sobolev, S. V. (2014). Rift migration explains continental margin asymmetry and crustal hyper-extension. *Nature Communications*, *5*(1), 4014. https://doi.org/10.1038/ncomms5014

Brune, S., Williams, S. E., & Müller, R. D. (2017). Potential links between continental rifting, CO_2 degassing and climate change through time. *Nature Geoscience*, *10*(12), 941–946. https://doi.org/10.1038/s41561-017-0003-6

Brune, S., Williams, S. E., & Müller, R. D. (2018). Oblique rifting: The rule, not the exception. *Solid Earth*, *9*(5), 1187–1206. https://doi.org/10.5194/se-9-1187-2018

Cammarano, F., Goes, S., Vacher, P., & Giardini, D. (2003). Inferring upper-mantle temperatures from seismic velocities. *Physics of the Earth and Planetary Interiors*, *138*(3–4), 197–222. https://doi.org/10.1016/S0031-9201(03)00156-0

Celli, N. L., Lebedev, S., Schaeffer, A. J., Ravenna, M., & Gaina, C. (2020). The upper mantle beneath the South Atlantic Ocean, South America and Africa from waveform tomography with massive data sets. *Geophysical Journal International*, *221*(1), 178–204. https://doi.org/10.1093/gji/ggz574

Chauvet, F., Sapin, F., Geoffroy, L., Ringenbach, J.-C., & Ferry, J.-N. (2021). Conjugate volcanic passive margins in the austral segment of the South Atlantic – Architecture and development. *Earth-Science Reviews*, *212*(B11), 103461. https://doi.org/10.1016/j.earscirev.2020.103461

Clemson, J., Cartwright, J., & Swart, R. (2007). The Namib Rift: A rift system of possible Karoo age, offshore Namibia. *Geological Society, London, Special Publications*, *153*(1), 381–402. https://doi.org/10.1144/GSL.SP.1999.153.01.23

Coffin, M., Duncan, R., Eldholm, O., Fitton, J. G., Frey, F., Larsen, H. C., et al. (2006). Large igneous provinces and scientific ocean drilling: Status quo and a look ahead. *Oceanography*, *19*(4), 150–160. https://doi.org/10.5670/oceanog.2006.13

Crameri, F. (2018). Geodynamic diagnostics, scientific visualisation and StagLab 3.0. *Geoscientific Model Development*, *11*(6), 2541–2562. https://doi.org/10.5194/gmd-11-2541-2018

EarthByte Group. (2022). *Rift subsidence*. Zenodo. https://doi.org/10.5281/zenodo.7074000

Evain, M., Afilhado, A., Rigoti, C., Loureiro, A., Alves, D., Klingelhoefer, F., et al. (2015). Deep structure of the Santos Basin-São Paulo plateau system, SE Brazil. *Journal of Geophysical Research: Solid Earth*, *120*(8), 5401–5431. https://doi.org/10.1002/2014JB011561

Finger, N.-P., Kaban, M. K., Tesauro, M., Haeger, C., Mooney, W. D., & Thomas, M. (2021). A thermo-compositional model of the cratonic lithosphere of South America. *Geochemistry, Geophysics, Geosystems*. https://doi.org/10.1029/2020GC009307

Franke, D. (2013). Rifting, lithosphere breakup and volcanism. Comparison of magma-poor and volcanic rifted margins. *Marine and Petroleum Geology*, *43*(4), 63–87. https://doi.org/10.1016/j.marpetgeo.2012.11.003

Geoffroy, L. (2005). Volcanic passive margins. *Comptes Rendus Geoscience*, *337*(16), 1395–1408. https://doi.org/10.1016/j.crte.2005.10.006

Heine, C., & Brune, S. (2014). Oblique rifting of the equatorial Atlantic: Why there is no Saharan Atlantic Ocean. *Geologica*, *42*(3), 211–214. https://doi.org/10.1130/G35082.1

Heine, C., Zoethout, J., & Müller, R. D. (2013). Kinematics of the South Atlantic rift. *Solid Earth*, *4*(2), 215–253. https://doi.org/10.5194/se-4-215-2013

Hunter, J. D. (2007). Matplotlib: A 2D graphics environment. *Computing in Science & Engineering*, *9*(3), 90–95. https://doi.org/10.1109/MCSE.2007.55

Jarvis, G. T., & McKenzie, D. P. (1980). Sedimentary basin formation with finite extension rates. *Earth and Planetary Science Letters*, *48*(1), 42–52. https://doi.org/10.1016/0012-821X(80)90168-5

Johansson, L., Zahirovic, S., & Müller, R. D. (2018). The interplay between the eruption and weathering of large igneous provinces and the deep-time carbon cycle. *Geophysical Research Letters*, *45*(11), 5380–5389. https://doi.org/10.1029/2017GL076691

Klöcking, M., Hoggard, M. J., Rodríguez Tribaldos, V., Richards, F. D., Guimarães, A. R., Maclennan, J., & White, N. J. (2020). A tale of two domes: Neogene to recent volcanism and dynamic uplift of northeast Brazil and southwest Africa. *Earth and Planetary Science Letters*, *547*(7), 116464. https://doi.org/10.1016/j.epsl.2020.116464

Laske, G., Masters, G., Ma, Z., & Pasyanos, M. (2013). Update on CRUST1.0 - A 1-degree global model of Earth's crust. *Geophysical Research Abstracts*, *15*.

Lister, G. S., Etheridge, M. A., & Symonds, P. A. (1986). Detachment faulting and the evolution of passive continental margins. *Geologica*, *14*(3), 246. https://doi.org/10.1130/0091-7613(1986)14<246:DFATEO>2.0.CO;2

McDermott, C., Lonergan, L., Collier, J. S., McDermott, K. G., & Bellingham, P. (2018). Characterization of seaward-dipping reflectors along the south American Atlantic margin and implications for continental breakup. *Tectonics*, *37*(9), 3303–3327. https://doi.org/10.1029/2017TC004923

McKenzie, D. (1978). Some remarks on the development of sedimentary basins. *Earth and Planetary Science Letters*, *40*(1), 25–32. https://doi.org/10.1016/0012-821X(78)90071-7

Morgan, J. P., Taramón, J. M., Araujo, M., Hasenclever, J., & Perez-Gussinye, M. (2020). Causes and consequences of asymmetric lateral plume flow during South Atlantic rifting. *Proceedings of the National Academy of Sciences of the United States of America*, *117*(45), 27877–27883. https://doi.org/10.1073/pnas.2012246117

Moulin, M., Aslanian, D., & Unternehr, P. (2010). A new starting point for the south and equatorial Atlantic Ocean. *Earth-Science Reviews*, *98*(1–2), 1–37. https://doi.org/10.1016/j.earscirev.2009.08.001

Müller, R. D., Cannon, J., Qin, X., Watson, R. J., Gurnis, M., Williams, S., et al. (2018). GPlates: Building a virtual Earth through deep time. *Geochemistry, Geophysics, Geosystems*, *19*(7), 2243–2261. https://doi.org/10.1029/2018GC007584

Müller, R. D., Zahirovic, S., Williams, S. E., Cannon, J., Seton, M., Bower, D. J., et al. (2019). A global plate model including lithospheric deformation along major rifts and orogens since the Triassic. *Tectonics*, *38*(6), 1884–1907. https://doi.org/10.1029/2018TC005462

Mutter, J. C., Talwani, M., & Stoffa, P. L. (1982). Origin of seaward-dipping reflectors in oceanic crust off the Norwegian margin by "subaerial sea-floor spreading". *Geologica*, *10*(7), 353. https://doi.org/10.1130/0091-7613(1982)10<353:OOSRIO>2.0.CO;2

Nielsen, T. K. (2002). Formation of volcanic rifted margins: Are temperature anomalies required? *Geophysical Research Letters*, *29*(21), 3623. https://doi.org/10.1029/2002GL015681

Parsons, B., & Sclater, J. G. (1977). An analysis of the variation of ocean floor bathymetry and heat flow with age. *Journal of Geophysical Research*, *82*(5), 803–827. https://doi.org/10.1029/JB082i005p00803

Pasyanos, M. E., Masters, T. G., Laske, G., & Ma, Z. (2014). LITHO1.0: An updated crust and lithospheric model of the Earth. *Journal of Geophysical Research: Solid Earth*, *119*(3), 2153–2173. https://doi.org/10.1002/2013JB010626

Peron-Pinvidic, G., & Manatschal, G. (2019). Rifted margins: State of the Art and future challenges. *Frontiers of Earth Science*, *7*, 601. https://doi.org/10.3389/feart.2019.00218

Peyve, A. A. (2010). Tectonics and magmatism in eastern South America and the Brazil Basin of the Atlantic in the Phanerozoic. *Geotectonics*, *44*(1), 60–75. https://doi.org/10.1134/S001685211001005X

Rabinowitz, P. D., & LaBrecque, J. (1979). The mesozoic South Atlantic Ocean and evolution of its continental margins. *Journal of Geophysical Research*, *84*(B11), 5973. https://doi.org/10.1029/JB084iB11p05973

Reston, T. J. (2009). The structure, evolution and symmetry of the magma-poor rifted margins of the North and Central Atlantic. A synthesis. *Tectonophysics*, *468*(1–4), 6–27. https://doi.org/10.1016/j.tecto.2008.09.002

Richards, F., Hoggard, M., Crosby, A., Ghelichkhan, S., & White, N. (2020). Structure and dynamics of the oceanic lithosphere-asthenosphere system. *Physics of the Earth and Planetary Interiors*, *309*, 106559. https://doi.org/10.1016/j.pepi.2020.106559

Ringrose, P. S., & Meckel, T. A. (2019). Maturing global CO_2 storage resources on offshore continental margins to achieve 2DS emissions reductions. *Scientific Reports*, *9*(1), 17944. https://doi.org/10.1038/s41598-019-54363-z

Robertson, C. G. (2017). CGG Robertson basin and plays. Retrieved from https://services3.arcgis.com/3wBYLDMc7IlzsBlJ/arcgis/rest/services/Basin_outlines_Robertson_Basins_and_Plays/FeatureServer

Schaeffer, A. J., & Lebedev, S. (2013). Global shear speed structure of the upper mantle and transition zone. *Geophysical Journal International*, *194*(1), 417–449. https://doi.org/10.1093/gji/ggt095

Sengör, A. M. C., & Burke, K. (1978). Relative timing of rifting and volcanism on Earth and its tectonic implications. *Geophysical Research Letters*, *5*(6), 419–421. https://doi.org/10.1029/GL005i006p00419

Simon, K., Huismans, R. S., & Beaumont, C. (2009). Dynamical modelling of lithospheric extension and small-scale convection. Implications for magmatism during the formation of volcanic rifted margins. *Geophysical Journal International*, *176*(1), 327–350. https://doi.org/10.1111/j.1365-246X.2008.03891.x

Steinberger, B., & Becker, T. W. (2018). A comparison of lithospheric thickness models. *Tectonophysics*, *746*, 325–338. https://doi.org/10.1016/j.tecto.2016.08.001

Straume, E. O., Gaina, C., Medvedev, S., Hochmuth, K., Gohl, K., Whittaker, J. M., et al. (2019). GlobSed: Updated total sediment thickness in the world's oceans. *Geochemistry, Geophysics, Geosystems*, *20*(4), 1756–1772. https://doi.org/10.1029/2018GC008115

Svartman Dias, A. E., Lavier, L. L., & Hayman, N. W. (2015). Conjugate rifted margins width and asymmetry: The interplay between lithospheric strength and thermomechanical processes. *Journal of Geophysical Research: Solid Earth*, *120*(12), 8672–8700. https://doi.org/10.1002/2015JB012074

Sykes, T. J. S. (1996). A correction for sediment load upon the ocean floor: Uniform versus varying sediment density estimations—Implications for isostatic correction. *Marine Geology*, *133*(1–2), 35–49. https://doi.org/10.1016/0025-3227(96)00016-3

Tugend, J., Gillard, M., Manatschal, G., Nirrengarten, M., Harkin, C., Epin, M.-E., et al. (2018). Reappraisal of the magma-rich versus magma-poor rifted margin archetypes. *Geological Society, London, Special Publications*, SP476.9. https://doi.org/10.1144/SP476.9

Turcotte, D., & Schubert, G. (2018). *Geodynamics*. Cambridge University Press.

Wernicke, B. (1981). Low-angle normal faults in the Basin and Range Province: Nappe tectonics in an extending orogen. *Nature*, *291*(5817), 645–648. https://doi.org/10.1038/291645a0

Williams, S. E., Whittaker, J. M., & Müller, R. D. (2011). Full-fit, palinspastic reconstruction of the conjugate Australian-Antarctic margins. *Tectonics*, *30*(6). https://doi.org/10.1029/2011TC002912

Zoback, M. L., & Mooney, W. D. (2010). Lithospheric buoyancy and continental intraplate stresses. *International Geology Review*, *45*(2), 95–118. https://doi.org/10.2747/0020-6814.45.2.95